Correlation-driven Lifshitz transition in electron-doped iron selenides (Li,Fe)OHFeSe

Da-Yong Liu,[1,*] Zhe Sun,[2] Feng Lu,[3] Wei-Hua Wang,[3] and Liang-Jian Zou[1]

[1]*Key Laboratory of Materials Physics, Institute of Solid State Physics, Chinese Academy of Sciences, P.O. Box 1129, Hefei, Anhui 230031, People's Republic of China*

[2]*National Synchrotron Radiation Laboratory, University of Science and Technology of China, Hefei, Anhui 230029, People's Republic of China*

[3]*Department of Electronic Science and Engineering, and Tianjin Key Laboratory of Photo-Electronic Thin Film Device and Technology, Nankai University, Tianjin 300071, People's Republic of China*

(Received 10 April 2018; revised manuscript received 17 September 2018; published 26 November 2018)

Effects of electronic correlation and spin-orbit coupling (SOC) on electronic structure of iron selenides $(Li_{1-x}Fe_x)$OHFeSe have been investigated with the combination of density functional theory (DFT) and dynamical mean-field theory. It is found that the electronic correlation substantially changes the Fermi surface topology for $x = 0.2$, resulting in a tiny electron pocket around the zone center Γ and two large electron pockets around the zone corner M, respectively. Moreover, the SOC also considerably affects the low-energy electronic structure near the Fermi level, especially inducing a gap in the Dirac-like dispersion around Γ for $x = 0.2$. Our calculations show a correlation-driven Lifshitz transition from FeSe to the heavily electron-doped compound, leading to a transition of the nesting wave vector from $(\pi, 0)$ to $(\pi, 0.5\pi \pm \delta)$ accompanied by an orbital-weight redistribution between the d_{xy} and d_{xz}/d_{yz} orbitals. These correlation-driven electronic structures enrich the understanding of different DFT and experimental results, suggesting a quite distinct superconducting state of $(Li_{0.8}Fe_{0.2})$OHFeSe in comparison with FeSe.

DOI: 10.1103/PhysRevB.98.195137

I. INTRODUCTION

Since the discovery of iron-based superconductors (FeSCs) in 2008 [1], a series of iron pnictides and chalcogenides, such as 1111 [1,2], 122 [3], 111 [4], 11 [5], and 112 [6] families, has been found. Although all of them contain the elementary unit of an FeAs layer or an FeSe layer, the multiorbital character of FeSCs, drastically different from the single-band cuprates, makes their phase diagrams more complicated. Moreover, these materials are regarded as correlated bad metals with moderate electronic correlation [7,8]. However, the correlated-metal behavior makes FeSCs different from both the conventional metal and the doped Mott insulator, which hinders the understanding of the electronic states and the superconductivity of these materials.

Among the iron-based materials, the FeSe-based compounds have been attracting great interest in recent years because of their surprisingly high superconducting transition temperature T_c. The T_c of the bulk FeSe can be enhanced from 8 to 37 K with applied pressure [5,9]. The intercalated FeSe compounds, such as $A_xFe_{2-y}Se_2$ (A = K, Cs, Rb, Tl, etc.), have $T_c \sim 30$ K [10]. More interesting, growing monolayer FeSe on $SrTiO_3$ substrate (FeSe/STO) can dramatically increase T_c above 65 K [11,12]. Though a series of FeSe-based compounds have been extensively studied experimentally and theoretically [13], the mechanism of the high T_c in iron selenides remains under debate. Especially, the Fe vacancies in $A_xFe_{2-y}Se_2$ and the complex interface effect in FeSe/STO make it more complicated to understand the superconductivity in these materials.

Recently, a new intercalated FeSe compound, i.e., $(Li_{1-x}Fe_x)$OHFeSe ($x \sim 0.2$), has been discovered with a high T_c of ~ 40 K [14–18]. Angle-resolved photoemission spectroscopy (ARPES) experiments show that the (Li,Fe)OH layer provides about 0.08–0.12 electrons per Fe for the FeSe layer [19,20]. Meanwhile, theoretical works have suggested that the intercalated $(Li_{1-x}Fe_x)$OH layer not only serves as a block or strain layer but also contributes to electron doping for the FeSe layer [21]. Therefore, $(Li_{1-x}Fe_x)$OHFeSe ($x \sim 0.2$) can be regarded as an electron-doped FeSe system, which makes it in line with FeSe/STO [22–25] and $A_xFe_{2-y}Se_2$ [26,27]. Since there are no Fe vacancies in $(Li_{1-x}Fe_x)$OHFeSe, it can be considered to be a reference material to investigate the superconductivity of heavily electron-doped FeSe-derived superconductors.

Although the electronic structure of $(Li_{1-x}Fe_x)$OHFeSe had been studied by ARPES and scanning tunneling microscopy (STM) experiments as well as density functional theory (DFT) calculations, there are still some discrepancies among different experiments and theoretical calculations. One puzzling issue is that a tiny electronic pocket around the Γ point in $(Li_{0.8}Fe_{0.2})$OHFeSe has been observed in ARPES [19,20] and STM [28] experiments, which is however not reproducible and instead has been replaced by two hole pockets within the DFT calculations [20,21]. Moreover, whether there exists a tiny electronic pocket around Γ or not is still unclear. For comparison, ARPES experiments have shown that around Γ there is no hole or electron pocket in FeSe/STO [29], while one small electron pocket emerges in $A_xFe_{2-y}Se_2$ [30]. On

*dyliu@theory.issp.ac.cn

the other hand, the Fermi surface nesting associated with hole and electron pockets plays a vital role in the spin excitation, spin-fluctuation-mediated superconducting pairing as well as in its pairing symmetry. Further investigation is thus needed to identify the Fermi surface topology of $(Li_{1-x}Fe_x)$OHFeSe. Actually, the discrepancy between experiments and DFT theoretical predictions may imply the importance of the electronic correlation in $(Li_{1-x}Fe_x)$OHFeSe. The constrained random-phase approximation result suggests that FeSe has a relatively large Coulomb interaction, U, and Hund's rule coupling, J_H [31,32]. In addition, ARPES experiments have reported that spin-orbit coupling (SOC) leads to an obvious modification of the electronic structure due to the presence of Dirac-like dispersion in FeSe [33,34]; it may also have a considerable effect on the topology of the Fermi surface in the electron-doped system $(Li_{1-x}Fe_x)$OHFeSe. Though the $(Li_{1-x}Fe_x)$OHFeSe compound seems to be an analog of the bulk FeSe, FeSe/STO, or even $A_{1-x}Fe_{2-y}Se_2$, the electronic correlation and multi-orbital physics make its electronic properties more complex. The key factor for the high superconducting transition temperature is still under debate in iron selenides, and the correlated electronic structure is the first step to address this issue.

In the present work, we have combined DFT and dynamical mean-field theory (DMFT) implemented with a continuous-time Monte Carlo (CT-QMC) impurity solver to investigate the influence of the electronic correlation and SOC in the electron-doped $(Li_{1-x}Fe_x)$OHFeSe compound in comparison with the FeSe system. It is found that the electronic structure is significantly modified by the electronic correlation in $(Li_{1-x}Fe_x)$OHFeSe at $x = 0.2$. The electronic correlations reshape the Fermi surface to a tiny electron pocket around Γ and two large electron pockets around M, resulting in a completely different Fermi surface topology with the absence of the hole pocket from other FeSe-based systems. Moreover, the SOC also partly contributes to the change of the electronic structure near the Fermi level. The novel Fermi surface without the hole pocket provides a realistic platform to investigate the role of the nesting in the pairing interaction in FeSCs. This paper is organized as follows: the crystal structure and calculated methods are described in Sec. II; then the DFT and DFT + DMFT results are presented in Secs. III and IV, respectively; and the last section is devoted to the conclusions.

II. CRYSTAL STRUCTURE AND NUMERICAL METHODS

In order to compare with the experimental data, the experimental crystal structure (low-temperature data) with the tetragonal space group $P4/nmm$ (No. 129) of $(Li_{1-x}Fe_x)$OHFeSe at $x = 0.2$ [15] is adopted. Notice that though FeSe has orthorhombic distortions at low temperature [35,36], in $(Li_{0.8}Fe_{0.2})$OHFeSe no evidence of an orthorhombic phase has been found experimentally. Since the electronic structure of the FeSe layer is our focus, for simplicity, an ideal LiOHFeSe crystal structure is constructed, in which the Fe atom in the (Li,Fe)OH layer is replaced by a Li atom and the structural parameters are maintained, as shown in Fig. 1. Accordingly, $x = 0$ corresponds to the LiOHFeSe system, while $x = 0.2$ represents the $(Li_{0.8}Fe_{0.2})$OHFeSe system with a shift of the Fermi level E_F to take into account the electron transfer from the $(Li_{0.8}Fe_{0.2})$OH layer to the FeSe layer. The

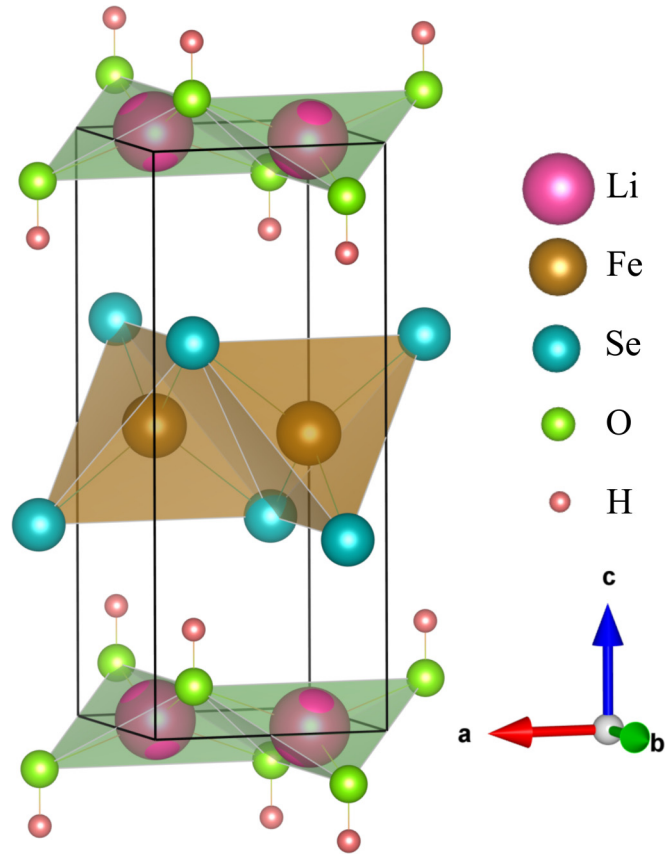

FIG. 1. Crystal structure of $(Li_{1-x}Fe_x)$OHFeSe at $x = 0$, drawn by VESTA software [37].

shift of E_F is determined by assuming that 0.2 electrons per formula unit in the $(Li_{0.8}Fe_{0.2})$OH layer are transferred to the Fe $3d$ orbitals of the FeSe layer [21]. In general, such electron doping from the intercalated layer leads to a rigid band shift, so the $x = 0.2$ case can be realized by a rigid band shift to take into account the electron doping. The validity of this rigid-band approximation had been verified by our previous study [21] and ARPES experiments [19,20,38].

Although the electronic structures of FeSCs are usually reproduced qualitatively by simple DFT calculations, the more quantitative agreement between calculations and ARPES data should be obtained by methods beyond DFT, such as DMFT, etc. Here we employ the DFT plus dynamical mean-field theory (DFT + DMFT) method implemented in embedded DMFT (EDMFT) code [39] to investigate the influence of the electronic correlation. The DFT + DMFT method is adopted to perform fully self-consistent charge calculations to explore the electronic structure of (Li,Fe)OHFeSe, which deals with the strong Coulomb interaction and the SOC on the same footing. Within the DFT + DMFT framework, the iterations can be split into two individual parts, DFT and DMFT. The DFT part is used to generate the Kohn-Sham Hamiltonian H_{KS}. The SOC is included in the Kohn-Sham Hamiltonian with a second variational treatment within the DFT framework. The DFT calculations are performed by the full-potential linearized augmented-plane-wave scheme based on DFT implemented with the WIEN2K software [40]. The generalized

gradient approximation by Perdew, Burke, and Ernzerhof [41] is used to take into account the exchange and correlation effects.

In the DMFT part, the DFT Hamiltonian H_{KS} is supplemented with a Coulomb interaction term, $H_{\rm int}$, for the correlated Fe $3d$ orbitals and a double counting term for self-energy function, $\Sigma_{\rm dc}$, and then the resulting multiorbital lattice model $H_{\rm DFT+DMFT} = H_{KS} + H_{\rm int} + \Sigma_{\rm dc}$ is solved utilizing the DMFT method. Based on the projection-embedding scheme implemented in EDMFT, the correlated Fe $3d$ electrons are treated dynamically with the DMFT local self-energy with atomic local basis (t_{2g} and e_g orbitals) projections, while the rest (s and p electrons) are treated on the DFT level. The impurity solver within the DMFT framework adopts the CT-QMC method [42] in the hybridization expansion. The exact double-counting correction based on the Luttinger-Ward functional is used [43]. We also tested the fully localized limit [44] scheme with the double-counting term $\Sigma_{\rm dc} = U(N_d - \frac{1}{2}) - \frac{J}{2}(N_d - 1)$, where N_d is the nominal electron occupancy of the correlated Fe $3d$ orbitals, which is updated dynamically during the DFT + DMFT iterations ($N_d = 6$ in the first iteration). Both schemes yield consistent results. The interaction parameters are used in the definition of the Slater integrals with the Coulomb parameter $U = F_0$ and the Hund's rule coupling $J = (F_2 + F_4)/14$ in its fully rotational invariant form. The parameters are adopted as $U = 5.0$ eV and $J = 0.8$ eV [31]. All the DMFT calculations are carried out at an inverse temperature of $\beta = 160\ \text{eV}^{-1}$ (about 72 K), which is higher than T_c; hence it is reasonable to consider only the paramagnetic solution. The DFT + DMFT computations are converged with respect to charge density, impurity level, chemical potential, self-energy, and lattice and impurity Green's functions. The maximum entropy method [45] is employed for the analytical continuation of the self-energy from the imaginary time and (Matsubara) frequency to real frequencies using an auxiliary Green's function. Then the momentum-resolved spectral functions, density of states, and optical conductivity can be obtained. In addition to the maximum entropy method, the Pade method is also used to check the stability and accuracy of our analytic continuation.

III. DFT RESULTS

We first investigate the electronic structure within DFT for (Li,Fe)OHFeSe. In order to examine the effect of SOC, the band structures without and with SOC are shown in Fig. 2. It is obvious that the electron doping from $x = 0$ to $x = 0.2$ leads to a significant change of the electronic structure near the Fermi level E_F. Notice that there are Dirac-like band dispersions around the Γ point, which have been also observed in other FeSCs [46]. Meanwhile, SOC also has a considerable effect. Indeed, the effect of SOC on the electronic structure has been observed by ARPES experiments in some FeSe-based compounds. For example, ARPES data show that SOC induces a gap around the M point in the FeSe/STO system [34]. In (Li,Fe)OHFeSe, a gap opening around the Γ point occurs due to SOC, where the Dirac-like dispersion is destroyed. In addition, the k_z dispersion is largely changed in the presence of SOC. All these imply that SOC may play an important role in electron-doped FeSe-based

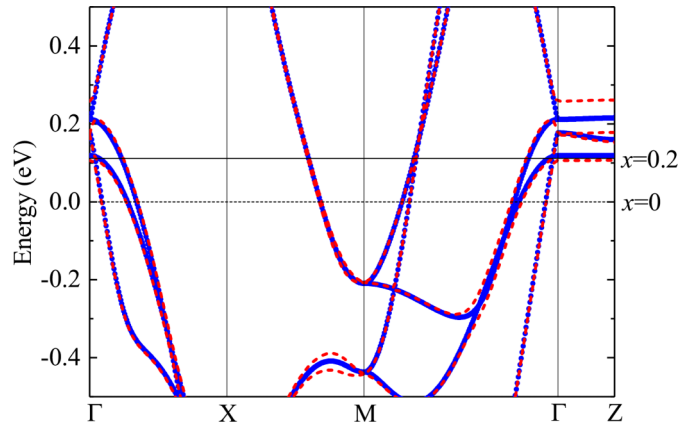

FIG. 2. Band structures of $(Li_{1-x}Fe_x)$OHFeSe without (blue solid line) and with (red dash line) SOC within DFT. The Fermi levels at $x = 0$ and $x = 0.2$ are presented, respectively.

materials. However, DFT calculations cannot reproduce the electronic structure observed by the ARPES experiments [20,21], and the electronic correlation may be responsible for this divergence.

IV. DFT + DMFT RESULTS

In order to examine the validity and reliability of the DFT + DMFT method, we applied the EDMFT to study the analog material FeSe at first. We had quantitatively reproduced the previous DFT + DMFT calculations of FeSe [47]. Moreover, our calculated results, such as momentum-resolved spectral function, Fermi surface, effective mass, and optical conductivity, are in good consistency with the experimental data. All these results are self-consistent both theoretically and experimentally and have proved the DFT + DMFT method is a reliable tool to describe the electronic structure of correlated iron-based materials.

Notice that the iron-based systems possess an intermediate electronic correlation, and different series of iron-based systems possess different strengths of the Coulomb interaction U and the Hund's rule coupling J_H. Among them, the Coulomb interaction U of iron selenides reaches the highest value, about 4–5 eV [31,32]. Therefore, the influence of the electronic correlation on the electronic structure of $(Li_{1-x}Fe_x)$OHFeSe may lead to a considerable renormalization effect. For comparison, the electronic structures without and with SOC are also calculated, respectively, within the DFT + DMFT framework.

A. Density of states

The total and projected Fe $3d$ orbital-resolved density of states (DOS) of (Li,Fe)OHFeSe are presented in Figs. 3(a) and 3(b), respectively. Compared with the DFT results [21], the correlated electronic structure produced by DFT + DMFT is very distinct, indicating that this system is a correlated bad metal. It is found that the Fermi level E_F lies in a dip structure of the DOS for both $x = 0$ and 0.2. Meanwhile, a van Hove singularity is located at E_F for $x = 0$, corresponding to LiOHFeSe, which is also observed in other iron-based

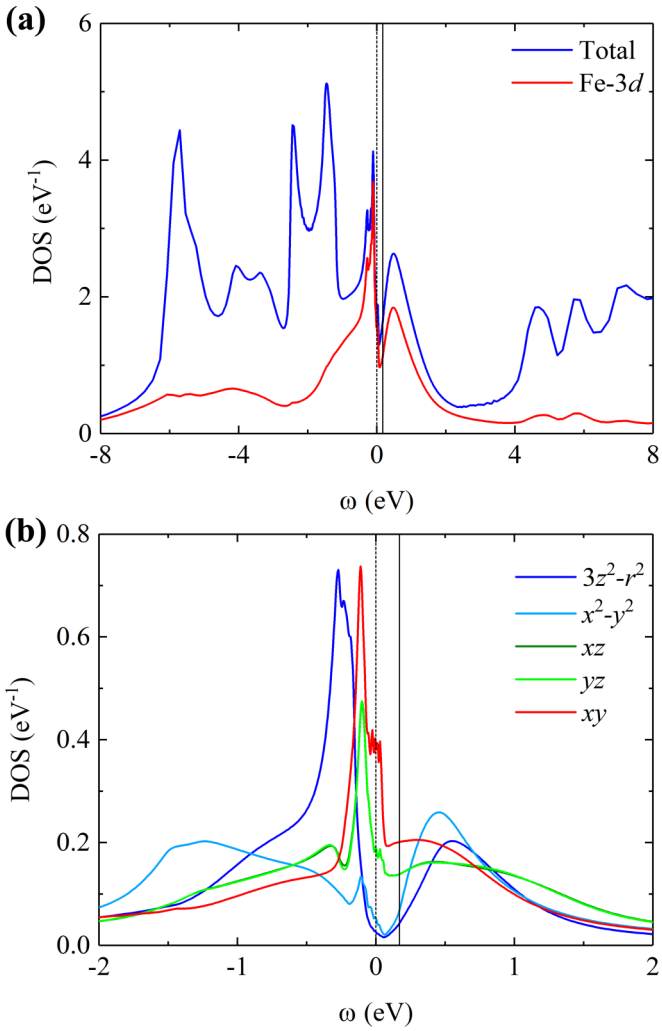

FIG. 3. (a) Total and (b) Fe $3d$ orbital-resolved density of states of (Li,Fe)OHFeSe without SOC within DFT + DMFT. The vertical dashed and solid lines denote the Fermi level at $x = 0$ and 0.2, respectively.

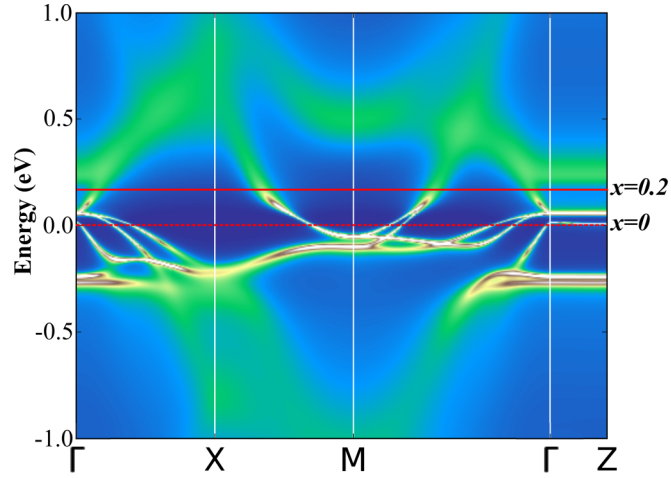

FIG. 4. Momentum-resolved spectral function of $(Li_{1-x}Fe_x)$OHFeSe without SOC within DFT + DMFT. The two horizontal lines correspond to $x = 0$ and 0.2, respectively.

materials. With the increase of electron doping from $x = 0$ to $x = 0.2$, E_F crosses the singularity and results in a sharp decrease of the total DOS in $(Li_{0.8}Fe_{0.2})$OHFeSe near the Fermi level. From $x = 0$ to this electron-doped system, the d_{xy} orbital weight, which is mainly contributed to the van Hove singularity, drops drastically in comparison with that of the d_{xz}/d_{yz} orbitals. Although the electron doping leads to a sharp change of the electronic structure, the Fe $3d$ orbital character is kept but with different weights, where the d_{xy} and degenerate d_{xz}/d_{yz} orbitals still dominate the low-energy physics in this compound [48]. This feature is in line with the orbital-selective Mott physics proposed in iron-based systems [49].

B. Spectral functions

To compare with the ARPES experiments, the momentum-resolved spectral function of (Li,Fe)OHFeSe without SOC is provided in Fig. 4. Different from the conventional DFT results, (Li,Fe)OHFeSe shows an obvious renormalized effect in the band structures due to electronic correlation. A characteristic Dirac-like dispersion shows up above E_F at the Γ point for $x = 0$ and sinks below E_F for $x = 0.2$. This undergoes a transition from a hole pocket to an electron one around the zone center Γ, indicating a correlation-driven Lifshitz transition. It is noted that 0.2 electrons per Fe doping from the $(Li_{0.8}Fe_{0.2})$OH layer is the ideal situation and that the realistic doping could be less than $0.2e$/Fe and leads to a small electron pocket around Γ or even its absence. On the other hand, the ARPES experiments are more sensitive to the top FeSe layer, where the doping could be affected in the absence of the (Li,Fe)OH layer on the top. These two factors likely contribute to the divergence between calculations and experiments. According to our calculation, there exists a critical doping concentration of $x_c \sim 0.08$, where the hole pocket vanishes while the electron pocket appears to correspond to the Dirac-like point at the Γ point. Considering that the calculated $x_c \sim 0.08$ is less than the estimated $0.1e$/Fe determined by the ARPES experiment [19], our results suggest the formation of the tiny electron pocket around the zone center Γ. Indeed, ARPES measurements of heavily electron-doped selenides, e.g., FeSe and $(Li_{0.8}Fe_{0.2})$OHFeSe with deposited K on the surface [38,50,51], also show this novel electronic structure with the new electron pocket around the Γ point.

Furthermore, the orbital-dependent electronic structure is shown in Fig. 5. It is evident that from $x = 0$ to 0.2 the orbital weight near E_F has a significant redistribution accompanied by an obvious change of the Fermi surface topology. At $x = 0.2$, the electron pocket around the Γ point is mainly dominated by a mixture of d_{xy} and d_{xz}/d_{yz} orbital characters (yellow color) with the former contributing a relatively larger weight than the latter. The electron pockets around the M point also contain a mixture of d_{xy} and d_{xz}/d_{yz} orbital character with $d_{xy} > d_{xz}/d_{yz}$ along M-Γ direction but $d_{xy} < d_{xz}/d_{yz}$ along the M-X direction. This indicates that when the electron is doped, the contribution from the d_{xy} and d_{xz}/d_{yz} orbitals becomes different from that of the pure FeSe system. Consequently, the change of the orbital character will possibly

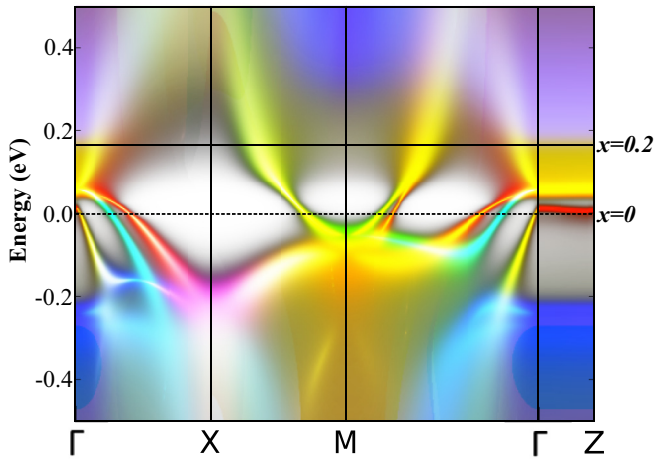

FIG. 5. Orbital-resolved spectral function of $(Li_{1-x}Fe_x)$OHFeSe without SOC within DFT + DMFT. The d_{xy} (red), d_{xz}/d_{yz} (green), $d_{x^2-y^2}$ and $d_{3z^2-r^2}$ (blue) orbital characters are highlighted in colors. The two horizontal lines correspond to $x = 0$ and 0.2, respectively.

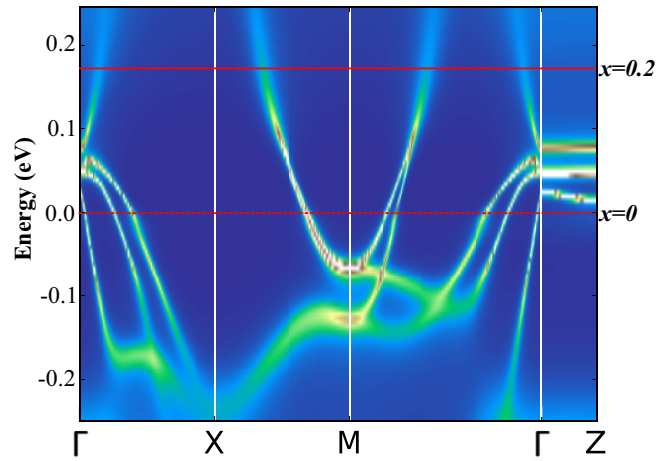

FIG. 6. Momentum-resolved spectral function of $(Li_{1-x}Fe_x)$OHFeSe with SOC within DFT + DMFT. The two horizontal lines correspond to $x = 0$ and 0.2, respectively.

lead to a completely different superconducting phase due to the different spin or orbital fluctuations.

Then the effect of SOC is presented in $(Li_{1-x}Fe_x)$OHFeSe. Notice that within DMFT, in the presence of SOC, the hybridization function becomes nondiagonal. Nevertheless, we can transform to a better local basis for the impurity solver. Due to the Monte Carlo sign problem with off-diagonal terms, we would rather change the orbital basis aligned with the local tetrahedron environment of the Fe atom to keep the density matrix maximally diagonal for the convenience of very efficient sampling with the Monte Carlo impurity solver. We have checked our hybridization function, which shows that at zero frequency we have completely diagonal hybridization, and also at infinity, the hybridization is much closer to diagonal. In addition, the analog material FeSe is calculated with our DFT + DMFT in the presence of SOC. We obtain consistent results compared with other previous works [47], indicating the reliability of our treatment. The momentum-resolved spectral function with SOC of (Li,Fe)OHFeSe is plotted in Fig. 6, showing that some degenerate bands are split due to the SOC. Especially, the Dirac-like dispersion around the Γ point is destroyed and a gap opens, which may affect the Lifshitz transition from the hole pocket to the electron one. Meanwhile, the k_z dispersion along Γ-Z shows a sharp change. These results illustrate the important role of SOC in FeSe-based systems [33].

C. Fermi surface and nesting

So far, $(Li_{1-x}Fe_x)$OHFeSe had been only synthesized experimentally with a fixed x doping parameter of about 0.2. To address the doping-dependent phase diagram, we can alternatively compare with the other two FeSe-based systems, i.e., FeSe and K-dosed $(Li_{0.8}Fe_{0.2})$OHFeSe, since the FeSe layer dominates the electronic properties. The experiment shows a low T_c of ~ 8 K for $x = 0$ (FeSe), an optimal T_c of ~ 43 K for $x = 0.2$ [$(Li_{0.8}Fe_{0.2})$OHFeSe], and a decreasing T_c for excessive doping $x > 0.2$ [K-dosed $(Li_{0.8}Fe_{0.2})$OHFeSe]. Combined with the doping-dependent evolution of the electronic structure, it evidently demonstrates the connection between Fermi surface topology and superconductivity. Since there is some inconsistency for the Fermi surface topology between the DFT calculations and the ARPES/STM experiments in $(Li_{1-x}Fe_x)$OHFeSe, the effect of electronic correlation within DFT + DMFT deserves to be investigated to address this issue. For comparison, the Fermi surfaces of both the DFT and the DFT + DMFT results at $x = 0$ are demonstrated in Figs. 7(a)–7(c). All the results give three hole pockets around the Γ point and two electron pockets around the M point, corresponding to LiOHFeSe [52], which is also consistent with that of the bulk FeSe within DFT + DMFT [47]. It indicates that the strain effect from the (Li,Fe)OH layer on the FeSe layer plays a minor role in the electronic structure. On the other hand, from Figs. 7(d)–7(f) at $x = 0.2$, once the electronic correlation is taken into account, the Fermi surface topology shows a considerable change, from two hole pockets to one electron pocket around the Γ point.

To explore the properties of the Fermi surface nesting, the bare susceptibility $\chi_0(q)$ is calculated within the DFT

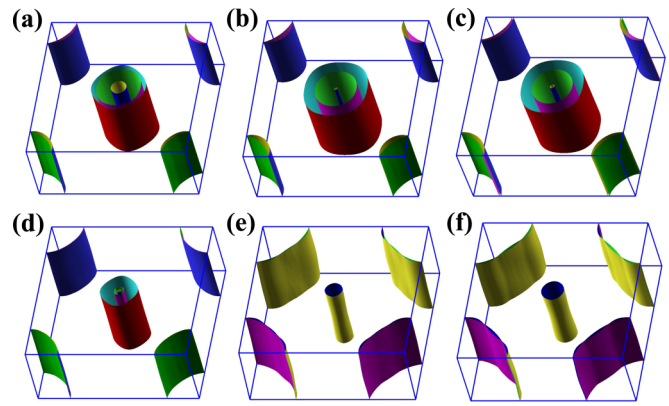

FIG. 7. Three-dimensional Fermi surface of $(Li_{1-x}Fe_x)$OHFeSe within DFT [panels (a) and (d)], DFT + DMFT [panels (b) and (e)], and DFT+DMFT+SOC [panels (c) and (f)] at $x = 0$ (LiOHFeSe) and $x = 0.2$ [$(Li_{0.8}Fe_{0.2})$OHFeSe], respectively.

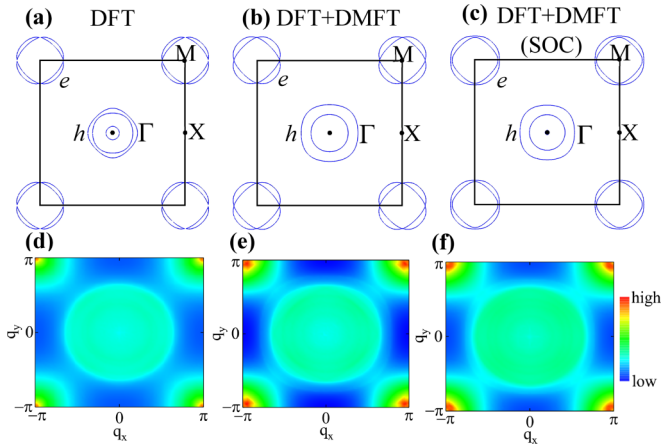

FIG. 8. Two-dimensional cut of the Fermi surface and the corresponding $\chi_0(q)$ of $(Li_{1-x}Fe_x)$OHFeSe within DFT [panels (a) and (d)], DFT + DMFT [panels (b) and (e)], and DFT + DMFT + SOC [panels (c) and (f)] at $x = 0$ (LiOHFeSe), respectively. The symbols e and h represent the electron and hole pockets, respectively.

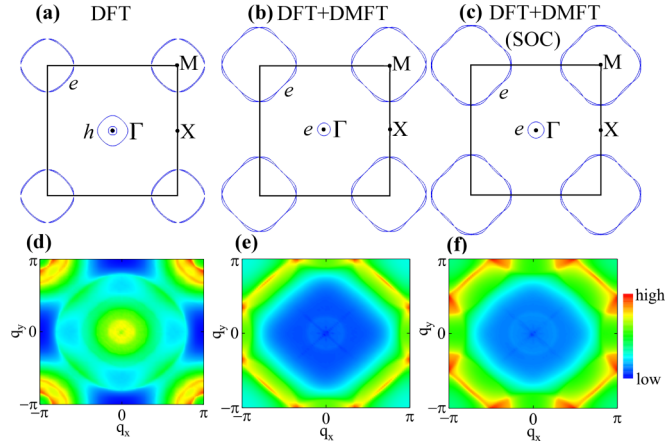

FIG. 9. Two-dimensional cut of the Fermi surface and the corresponding $\chi_0(q)$ of $(Li_{1-x}Fe_x)$OHFeSe within DFT [panels (a) and (d)], DFT + DMFT [panels (b) and (e)], and DFT + DMFT + SOC [panels (c) and (f)] at $x = 0.2$ [$(Li_{0.8}Fe_{0.2})$OHFeSe], respectively. The symbols e and h represent the electron and hole pockets, respectively.

framework by [26,46,53]

$$\chi^0_{\alpha\alpha'\beta\beta'}(q) = -\frac{1}{N}\sum_{\vec{k},n,m} |M_{kn,k+qm}|^2_{\alpha\alpha'\beta\beta'} \times \frac{f[\varepsilon_m(\vec{k}+\vec{q})] - f[\varepsilon_n(\vec{k})]}{\varepsilon_m(\vec{k}+\vec{q}) - \varepsilon_n(\vec{k}) + i\eta}, \quad (1)$$

with matrix elements $|M_{kn,k+qm}|^2_{\alpha\alpha'\beta\beta'} = a_n^{\beta'}(k)a_n^{\alpha',*}(k)$ $a_m^{\alpha}(k+q)a_m^{\beta,*}(k+q)$ represented by the orbital projection of the Bloch state, and the parameter $\eta = 0.001$ enforces analyticity in the sum over Matsubara frequencies. Note that to better understand the role of Fermi surface nesting alone, the orbital matrix elements in the bare susceptibility are suppressed for the DFT calculations. Though matrix elements often are important, evaluations without matrix elements are much more common [46]. It is evident that that the consideration of the orbital matrix elements does not change the nesting wave vector but rather the peak intensity for iron-based materials [26,46,53–55]. Consequently the nesting feature can be checked by examining the bare electronic susceptibility for convenience. Within the DMFT framework, χ_0 is given as the convolution of the fully interacting one-particle Green's function,

$$\chi^0_{\alpha\alpha'\beta\beta'}(q) = -\frac{T}{N}\sum_{\vec{k}} G_{\beta\alpha}(k)G_{\alpha'\beta'}(k+q). \quad (2)$$

The Green functions are connected with the spectral function by $A(k,\omega) = -\frac{1}{\pi}\mathrm{Im}G(k,\omega)$. Note that the two-particle vertex correction is omitted, since it mainly amplifies the susceptibility intensity while preserving the q dependence [56,57]. Figures 8(d)–8(f) show $\chi_0(q)$ based on three different electronic structures for $(Li_{1-x}Fe_x)$OHFeSe, i.e., DFT, DFT + DMFT, and DFT + DMFT + SOC, respectively. It is peaked at $\mathbf{q} = (\pi, \pi)$ in the 2-Fe Brillouin zone (corresponding to $(\pi, 0)$ in the 1-Fe Brillouin zone [58]) at $x = 0$. The obtained nesting wave vector $\mathbf{q}$ is consistent with previous results of pure FeSe [59–61] and FeAs-based systems [53,62]. When both the electronic correlation and the SOC are taken into account, the peak position shifts a little away from (π, π), indicating a robust Fermi surface nesting.

On the other hand, the Fermi surface for the $x = 0.2$ system has a significant change due to the electronic correlation, as shown in Figs. 7(d)–7(f). The two hole pockets around the Γ point are replaced by one small electron pocket, which is purely electron correlation driven. It is consistent with the ARPES [19,20] and STM [28] measurements, which also explains the puzzling observation of Γ-M scattering in the STM experiment [28]. Apart from the change around the zone center Γ, the two nearly degenerate electron pockets around the zone corner M become significantly large. In general, DFT calculations can correctly produce the Fermi surface topology of the iron-based materials, but fail in $(Li_{0.8}Fe_{0.2})$OHFeSe. Since the hole pocket around Γ is eliminated in FeSe/STO [20] or even replaced by the electron pocket in $K_{1-x}Fe_{2-y}Se_2$ [20,26,63] induced by the electron doping, the correlation-driven change of the carrier type of the pocket around the zone center in $(Li_{0.8}Fe_{0.2})$OHFeSe provides a reference with novel Fermi surface topology for the understanding of the unconventional superconductivity in FeSCs. Consequently, this can be used to verify the superconducting pairing symmetry based on the Fermi surface nesting scenario, which is still under hot debate.

Accordingly, $\chi_0(q)$ of the electron-doped system $(Li_{0.8}Fe_{0.2})$OHFeSe is also shown in Figs. 9(d)–9(f) for DFT, DFT + DMFT, and DFT + DMFT + SOC calculations. Compared with the $x = 0$ system, it is peaked relatively far away from (π, π) for the $x = 0.2$ system. In the DFT case, it is peaked at $(\pi, 0.84\pi)$. While from the DMFT case to the DMFT + SOC case, the peak shifts from $(\pi, 0.34\pi)$ to $(\pi, 0.48\pi)$. Considering both the electronic correlation and the SOC, the peak of χ_0 becomes close to $(\pi, 0.5\pi \pm \delta)$ and $(0.5\pi \pm \delta, 0.5\pi \pm \delta)$ in the 2-Fe Brillouin zone, corresponding to $(0.75\pi \mp \delta, 0.25\pi \pm \delta)$ and $(\pi,$

TABLE I. Effective mass m^*/m_{DFT} of Fe $3d$ orbitals for (Li,Fe)OHFeSe within DFT + DMFT.

Orbitals d_{xz}/d_{yz}	d_{xy}	$d_{x^2-y^2}$	$d_{3z^2-r^2}$
m^*/m_{DFT} 3.01	4.43	2.07	2.11

$0.5\pi \pm \delta$) in the 1-Fe Brillouin zone. The obtained wave vector is very close to the neutron-scattering experimental value (π, 0.62π) [64,65], which is in the vicinity of (π, 0.5π) as observed in other intercalated FeSe compounds [66,67]. According to our calculations, the deviation δ is determined by the size of the electron pocket around the zone corner, which is dependent on the electron doping level. Since the electron doping is overestimated in the ideal case, the calculated electron pocket is relatively larger than the experimental observation, resulting in a considerable deviation δ. These results imply the importance of the interplay among Fermi surface nesting, electronic correlation, and SOC in iron-based systems.

We emphasize that the absence of the hole pocket around Γ observed experimentally in $A_xFe_{2-y}Se_2$ and (Li,Fe)OHFeSe has ruled out the possibility of the nesting scenario in iron-based superconductors, though sometimes it seems to be valid. According to our calculated results and previous works, the electronic correlation or interaction also plays an essential role in the superconducting pairing state of iron-based systems. The nesting alone is insufficient to induce sufficiently strong spin and orbital fluctuations responsible for the high T_c superconductivity in iron-based materials. On the other hand, the topology of the Fermi surface is also greatly changed by the electronic correlation or interaction, and its nesting wave vector is strongly dependent on the strength of the interaction. Therefore both the nesting and the interaction contribute to the superconductivity of iron-based materials.

D. Effective mass

To study the band structure renormalization of each Fe $3d$ orbital, the orbital-resolved self-energies $\Sigma_\alpha(\omega)$ within DFT + DMFT are calculated through the analytical continuation with the maximum entropy method. The different orbitals have different self-energies for both the real part $\mathrm{Re}\Sigma(\omega)$ and the imaginary part $\mathrm{Im}\Sigma(\omega)$ of the self-energies. As we know, the quasiparticle weight is calculated as $Z_\alpha = (1 - \frac{\partial \Sigma_\alpha}{\partial i\omega})^{-1}|_{i\omega\to 0}$, and $m^*/m_{DFT} = 1/Z = 1 - \frac{\partial Re\Sigma(\omega)}{\partial \omega}|_{\omega=0}$. Through analysis of the self-energy Σ, the effective mass m^* of Fe $3d$ orbitals is obtained. The effective mass m^*/m_{DFT} values of Fe $3d$ orbitals for (Li,Fe)OHFeSe within DFT + DMFT are listed in Table I. It is found that the d_{xy} orbital has the largest effective mass $m^*/m_{DFT} = 4.4$ compared with the value of 3.01 of the d_{xz}/d_{yz} orbitals. Obviously, the relative magnitudes of the effective masses of different orbitals are consistent with that of the bulk FeSe within DFT + DMFT [68,69], but there is a relatively weak renormalization in (Li,Fe)OHFeSe. The calculated average effective mass is about 2.93, consistent with the experimental value of 2.9 [20], which assesses the accuracy and reliability of our calculations.

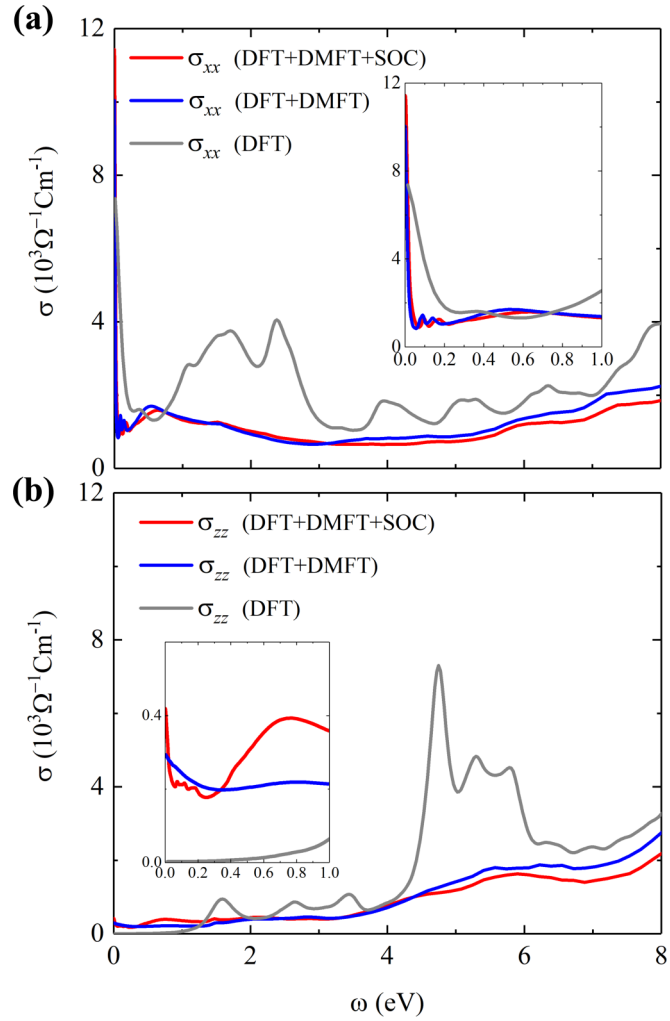

FIG. 10. Real part of in-plane (a) and out-plane (b) optical conductivities of (Li,Fe)OHFeSe obtained by both DFT and DFT + DMFT methods. Insets: Magnified views of the optical conductivity at low frequencies.

E. Optical conductivity

To capture the many-body effect induced by electronic correlation, we have also calculated the optical conductivity of (Li,Fe)OHFeSe using both DFT and DFT + DMFT methods. In the calculations of the optical conductivity $\sigma_{\alpha\alpha}(\omega)$ along the α direction, different formulas were adopted for DFT [70] and DFT + DMFT [71] methods, which are implemented in WIEN2K and EDMFT codes, respectively. In DMFT, the optical conductivity is calculated using the self-energy on the real frequency axis from the maximum entropy method. The calculated in-plane and out-plane optical conductivities of (Li,Fe)OHFeSe within DFT, DFT + DMFT, and DFT + DMFT + SOC are plotted for comparison in Figs. 10(a) and 10(b), respectively. However, the experimental results of the optical conductivity for (Li,Fe)OHFeSe have not yet been reported. Notice that the optical conductivity of its analog material FeSe had been reported theoretically and experimentally [47,72–74]. In order to check our calculated method based on DMFT, we calculate the conductivity of FeSe at first and obtain a consistent result with the previous theoretical work

and experimental data [47,72,73], indicating our calculations are reliable. We compared these two FeSe-based materials and found that (Li,Fe)OHFeSe shows a roughly distinct optical conductivity in comparison with bulk FeSe [74], though they share similar Drude features. Nevertheless, the optical conductivity of (Li,Fe)OHFeSe is very similar to that of the FeSe film on the substrate $SrTiO_3$ (also an electron-doped FeSe) [72].

As expected for metals, all the spectra exhibit clear Drude-like responses. The DMFT calculations show significantly reduced spectral weight compared to the DFT values at low frequency, showing the importance of the correlation effect. From Fig. 10(a), it is found that the low-frequency in-plane optical spectrum within DFT + DMFT mainly consists of two components: a narrow Drude one accounts for the coherent itinerant carrier (intraband) response, and a broad Lorentz one represents the incoherent localized (interband) excitations. The sharp Drude component at low frequencies was not observed in iron pnictide materials, implying a completely different band renormalization due to the many-body correlated effect in iron selenides at low temperature. The out-plane Drude response in DMFT is also very different from the DFT calculations, as shown in Fig. 10(b). In addition, there is clearly a correlation between the SOC and the Drude peak strength, suggesting that SOC also plays a key role in the optical response.

V. CONCLUSIONS

In summary, the electronic correlation and spin-orbit coupling in (Li,Fe)OHFeSe have been investigated using the DFT + DMFT method implemented with the CT-QMC impurity solver. A correlation-driven electronic structure accompanied by a Lifshitz transition is found in electron-doped (Li,Fe)OHFeSe, indicating a superconducting phase completely different from that in the bulk FeSe. Both the electronic correlation and the spin-orbit coupling play key roles in the electronic structure of electron-doped selenides $(Li_{1-x}Fe_x)$OHFeSe, which induce a small electron pocket around Γ as observed by recent ARPES measurements on K-dosed $(Li_{0.8}Fe_{0.2})$OHFeSe. All these results are in good qualitative agreement with the experimental ARPES data, which demonstrate the many-body characteristics, such as many-body self-energy, coherent spectral weight, strong damping of quasiparticles in the vicinity of the Fermi level, and a strong renormalization of the effective masses. Further explorations on the superconductivity of (Li,Fe)OHFeSe needs to consider the novel Fermi surface topology with only electron pockets. In particular, the tiny electron pocket around the zone center should be taken into account, since it provides a Γ-M scattering channel as observed in recent STM studies. Our studies suggest that the electron-doped selenides $(Li_{1-x}Fe_x)$OHFeSe could be an ideal system to identify the role of electronic correlation and spin-orbit coupling in superconductivity of iron-based materials.

ACKNOWLEDGMENTS

The authors gratefully acknowledge the valuable discussions with Dr. Guoren Zhang. This work was supported by the National Science Foundation of China under Grants No. 11574315, No. 11190022, No. 11404172, and No. 11474287 and the Key Research Program of the Chinese Academy of Sciences (Grant No. XDPB01). Numerical calculations were performed at the Center for Computational Science of CASHIPS and the ScGrid of Supercomputing Center and Computer Network Information Center of the Chinese Academy of Sciences.

[1] Y. Kamihara, T. Watanabe, M. Hirano, and H. Hosono, J. Am. Chem. Soc. **130**, 3296 (2008).
[2] X. H. Chen, T. Wu, G. Wu, R. H. Liu, H. Chen, and D. F. Fang, Nature (London) **453**, 761 (2008).
[3] M. Rotter, M. Tegel, and D. Johrendt, Phys. Rev. Lett. **101**, 107006 (2008).
[4] J. H. Tapp, Z. Tang, B. Lv, K. Sasmal, B. Lorenz, P. C. W. Chu, and A. M. Guloy, Phys. Rev. B **78**, 060505(R) (2008).
[5] F. C. Hsu, J. Y. Luo, K. W. Yeh, T. K. Chen, T. W. Huang, P. M. Wu, Y. C. Lee, Y. L. Huang, Y. Y. Chu, D. C. Yan, and M. K. Wu, Proc. Natl. Acad. Sci. U.S.A. **105**, 14262 (2008).
[6] N. Katayama, K. Kudo, S. Onari, T. Mizukami, K. Sugawara, Y. Sugiyama, Y. Kitahama, K. Iba, K. Fujimura, N. Nishimoto, M. Nohara, and H. Sawa, J. Phys. Soc. Jpn. **82**, 123702 (2013).
[7] M. M. Qazilbash, J. J. Hamlin, R. E. Baumbach, L. J. Zhang, D. J. Singh, M. B. Maple, and D. N. Basov, Nat. Phys. **5**, 647 (2009).
[8] K. Haule, J. H. Shim, and G. Kotliar, Phys. Rev. Lett. **100**, 226402 (2008).
[9] S. Margadonna, Y. Takabayashi, Y. Ohishi, Y. Mizuguchi, Y. Takano, T. Kagayama, T. Nakagawa, M. Takata, and K. Prassides, Phys. Rev. B **80**, 064506 (2009).
[10] J. G. Guo, S. F. Jin, G. Wang, S. C. Wang, K. X. Zhu, T. T. Zhou, M. He, and X. L. Chen, Phys. Rev. B **82**, 180520(R) (2010).
[11] S. L. He *et al.*, Nat. Mater. **12**, 605 (2013).
[12] J. F. Ge, Z. L. Liu, C. H. Liu, C. L. Gao, D. Qian, Q. K. Xue, Y. Liu, and J. F. Jia, Nat. Mater. **14**, 285 (2015).
[13] E. Dagotto, Rev. Mod. Phys. **85**, 849 (2013).
[14] X. F. Lu, N. Z. Wang, G. H. Zhang, X. G. Luo, Z. M. Ma, B. Lei, F. Q. Huang, and X. H. Chen, Phys. Rev. B **89**, 020507(R) (2014).
[15] X. F. Lu, N. Z. Wang, H. Wu, Y. P. Wu, D. Zhao, X. Z. Zeng, X. G. Luo, T. Wu, W. Bao, G. H. Zhang, F. Q. Huang, Q. Z. Huang, and X. H. Chen, Nat. Mater. **14**, 325 (2015).
[16] U. Pachmayr, F. Nitsche, H. Luetkens, S. Kamusella, F. Brückner, R. Sarkar, H. H. Klauss, and D. Johrendt, Angew. Chem., Int. Ed. **54**, 293 (2015).
[17] H. L. Sun, D. N. Woodruff, S. J. Cassidy, G. M. Allcroft, S. J. Sedlmaier, A. L. Thompson, P. A. Bingham, S. D. Forder, S. Cartenet, N. Mary, S. Ramos, F. R. Foronda, B. H. Williams, X. D. Li, S. J. Blundell, and S. J. Clarke, Inorg. Chem. **54**, 1958 (2015).
[18] X. L. Dong, H. X. Zhou, H. X. Yang, J. Yuan, K. Jin, F. Zhou, D. N. Yuan, L. L. Wei, J. Q. Li, X. Q. Wang, G. M. Zhang, and Z. X. Zhao, J. Am. Chem. Soc. **137**, 66 (2015).
[19] X. H. Niu, R. Peng, H. C. Xu, Y. J. Yan, J. Jiang, D. F. Xu, T. L. Yu, Q. Song, Z. C. Huang, Y. X. Wang, B. P. Xie, X. F. Lu,

N. Z. Wang, X. H. Chen, Z. Sun, and D. L. Feng, Phys. Rev. B **92**, 060504(R) (2015).
[20] L. Zhao *et al.*, Nat. Commun. **7**, 10608 (2016).
[21] D. Y. Liu, Z. Sun, and L. J. Zou, New J. Phys. **19**, 023028 (2017).
[22] J. Bang, Z. Li, Y. Y. Sun, A. Samanta, Y. Y. Zhang, W. Zhang, L. Wang, X. Chen, X. Ma, Q.-K. Xue, and S. B. Zhang, Phys. Rev. B **87**, 220503 (2013).
[23] K. V. Shanavas and D. J. Singh, Phys. Rev. B **92**, 035144 (2015).
[24] K. Zou, S. Mandal, S. D. Albright, R. Peng, Y. Pu, D. Kumah, C. Lau, G. H. Simon, O. E. Dagdeviren, X. He, I. Božović, U. D. Schwarz, E. I. Altman, D. Feng, F. J. Walker, S. Ismail-Beigi, and C. H. Ahn, Phys. Rev. B **93**, 180506 (2016).
[25] S. Mandal, P. Zhang, S. Ismail-Beigi, and K. Haule, Phys. Rev. Lett. **119**, 067004 (2017).
[26] D.-Y. Liu, Y.-M. Quan, Z. Zeng, and L.-J. Zou, Physica B **407**, 1139 (2012).
[27] T. Qian, X. P. Wang, W. C. Jin, P. Zhang, P. Richard, G. Xu, X. Dai, Z. Fang, J. G. Guo, X. L. Chen, and H. Ding, Phys. Rev. Lett. **106**, 187001 (2011).
[28] Y. J. Yan, W. H. Zhang, M. Q. Ren, X. Liu, X. F. Lu, N. Z. Wang, X. H. Niu, Q. Fan, J. Miao, R. Tao, B. P. Xie, X. H. Chen, T. Zhang, and D. L. Feng, Phys. Rev. B **94**, 134502 (2016).
[29] D. F. Liu *et al.*, Nat. Commun. **3**, 931 (2012).
[30] D. X. Mou *et al.*, Phys. Rev. Lett. **106**, 107001 (2011).
[31] Z. P. Yin, K. Haule, and G. Kotliar, Nat. Mater. **10**, 932 (2011).
[32] T. Miyake, K. Nakamura, R. Arita, and M. Imada, J. Phys. Soc. Jpn. **79**, 044705 (2010).
[33] S. V. Borisenko, D. V. Evtushinsky, Z. H. Liu, I. Morozov, R. Kappenberger, S. Wurmehl, B. Büchner, A. N. Yaresko, T. K. Kim, M. Hoesch, T. Wolf, and N. D. Zhigadlo, Nat. Phys. **12**, 311 (2016).
[34] Z. F. Wang, H. M. Zhang, D. F. Liu, C. Liu, C. J. Tang, C. L. Song, Y. Zhong, J. P. Peng, F. S. Li, C. N. Nie, L. L. Wang, X. J. Zhou, X. C. Ma, Q. K. Xue, and F. Liu, Nat. Mater. **15**, 968 (2016).
[35] A. E. Böhmer, F. Hardy, F. Eilers, D. Ernst, P. Adelmann, P. Schweiss, T. Wolf, and C. Meingast, Phys. Rev. B **87**, 180505(R) (2013).
[36] A. Fedorov, A. Yaresko, T. K. Kim, Y. Kushnirenko, E. Haubold, T. Wolf, M. Hoesch, A. Grüneis, B. Büchner, and S. V. Borisenko, Sci. Rep. **6**, 36834 (2016).
[37] K. Momma and F. Izumi, J. Appl. Crystallogr. **44**, 1272 (2011).
[38] M. Q. Ren, Y. J. Yan, X. H. Niu, R. Tao, D. Hu, R. Peng, B. P. Xie, J. Zhao, T. Zhang, and D. L. Feng, Sci. Adv. **3**, e1603238 (2017).
[39] K. Haule, C. H. Yee, and K. Kim, Phys. Rev. B **81**, 195107 (2010).
[40] P. Blaha, K. Schwarz, G. Madsen, D. Kvasnicka, and J. Luitz, *Computer Code WIEN2K: An Augmented Plane Wave plus Local Orbitals Program for Calculating Crystal Properties* (Karlheinz Schwarz, Technische Universität Wien, Austria, 2001).
[41] J. P. Perdew, K. Burke, and M. Ernzerhof, Phys. Rev. Lett. **77**, 3865 (1996).
[42] K. Haule, Phys. Rev. B **75**, 155113 (2007).
[43] K. Haule, Phys. Rev. Lett. **115**, 196403 (2015).
[44] V. I. Anisimov, F. Aryasetiawan, and A. I. Lichtenstein, J. Phys.: Condens. Matter **9**, 767 (1997).
[45] M. Jarrell and J. E. Gubernatis, Phys. Rep. **269**, 133 (1996).
[46] Y. N. Huang, D. Y. Liu, L. J. Zou, and W. E. Pickett, Phys. Rev. B **93**, 195148 (2016).
[47] S. Mandal, R. E. Cohen, and K. Haule, Phys. Rev. B **89**, 220502(R) (2014).
[48] D. Y. Liu, Y. M. Quan, D. M. Chen, L. J. Zou, and H. Q. Lin, Phys. Rev. B **84**, 064435 (2011).
[49] L. de' Medici, G. Giovannetti, and M. Capone, Phys. Rev. Lett. **112**, 177001 (2014).
[50] C. H. P. Wen, H. C. Xu, C. Chen, Z. C. Huang, X. Lou, Y. J. Pu, Q. Song, B. P. Xie, M. Abdel-Hafiez, D. A. Chareev, A. N. Vasiliev, R. Peng, and D. L. Feng, Nat. Commun. **7**, 10840 (2016).
[51] X. Shi, Z. Q. Han, X. L. Peng, P. Richard, T. Qian, X. X. Wu, M. W. Qiu, S. C. Wang, J. P. Hu, Y. J. Sun, and H. Ding, Nat. Commun. **8**, 14988 (2017).
[52] A. Subedi, L. J. Zhang, D. J. Singh, and M. H. Du, Phys. Rev. B **78**, 134514 (2008).
[53] S. Graser, T. A. Maier, P. J. Hirschfeld, and D. J. Scalapino, New J. Phys. **11**, 025016 (2009).
[54] G. Lee, H. S. Ji, Y. Kim, C. Kim, K. Haule, G. Kotliar, B. Lee, S. Khim, K. H. Kim, K. S. Kim, K.-S. Kim, and J. H. Shim, Phys. Rev. Lett. **109**, 177001 (2012).
[55] Y. Li, Z. P. Yin, X. C. Wang, D. W. Tam, D. L. Abernathy, A. Podlesnyak, C. L. Zhang, M. Wang, L. Y. Xing, C. Q. Jin, K. Haule, G. Kotliar, T. A. Maier, and P. C. Dai, Phys. Rev. Lett. **116**, 247001 (2016).
[56] D. W. Tam *et al.*, Phys. Rev. B **95**, 060505(R) (2017).
[57] Z. P. Yin, K. Haule, and G. Kotliar, Nat. Phys. **10**, 845 (2014).
[58] S. Kong, D. Y. Liu, S. T. Cui, S. L. Ju, A. F. Wang, X. G. Luo, L. J. Zou, X. H. Chen, G. B. Zhang, and Z. Sun, Phys. Rev. B **92**, 184512 (2015).
[59] M. C. Rahn, R. A. Ewings, S. J. Sedlmaier, S. J. Clarke, and A. T. Boothroyd, Phys. Rev. B **91**, 180501(R) (2015).
[60] A. Kreisel, S. Mukherjee, P. J. Hirschfeld, and B. M. Andersen, Phys. Rev. B **92**, 224515 (2015).
[61] Q. S. Wang, Y. Shen, B. Y. Pan, Y. Q. Hao, M. W. Ma, F. Zhou, P. Steffens, K. Schmalzl, T. R. Forrest, M. Abdel-Hafiez, X. J. Chen, D. A. Chareev, A. N. Vasiliev, P. Bourges, Y. Sidis, H. B. Cao, and J. Zhao, Nat. Mater. **15**, 159 (2016).
[62] K. Kuroki, S. Onari, R. Arita, H. Usui, Y. Tanaka, H. Kontani, and H. Aoki, Phys. Rev. Lett. **101**, 087004 (2008).
[63] D. Y. Liu, Y. M. Quan, X. J. Zheng, X. L. Yu, and L. J. Zou, J. Phys.: Condens. Matter **25**, 125601 (2013).
[64] N. R. Davies, M. C. Rahn, H. C. Walker, R. A. Ewings, D. N. Woodruff, S. J. Clarke, and A. T. Boothroyd, Phys. Rev. B **94**, 144503 (2016).
[65] B. Y. Pan, Y. Shen, D. Hu, Y. Feng, J. T. Park, A. D. Christianson, Q. S. Wang, Y. Q. Hao, H. L. Wo, Z. P. Yin, T. A. Maier, and J. Zhao, Nat. Commun. **8**, 123 (2017).
[66] A. E. Taylor, S. J. Sedlmaier, S. J. Cassidy, E. A. Goremychkin, R. A. Ewings, T. G. Perring, S. J. Clarke, and A. T. Boothroyd, Phys. Rev. B **87**, 220508(R) (2013).
[67] T. A. Maier, S. Graser, P. J. Hirschfeld, and D. J. Scalapino, Phys. Rev. B **83**, 100515(R) (2011).
[68] M. Aichhorn, S. Biermann, T. Miyake, A. Georges, and M. Imada, Phys. Rev. B **82**, 064504 (2010).

[69] I. Leonov, S. L. Skornyakov, V. I. Anisimov, and D. Vollhardt, Phys. Rev. Lett. **115**, 106402 (2015).
[70] C. A. Draxla and J. O. Sofo, Comput. Phys. Commun. **175**, 1 (2006).
[71] D. N. Basov, R. D. Averitt, D. van der Marel, M. Dressel, and K. Haule, Rev. Mod. Phys. **83**, 471 (2011).
[72] R. H. Yuan, W. D. Kong, L. Yan, H. Ding, and N. L. Wang, Phys. Rev. B **87**, 144517 (2013).
[73] M. Nakajima, K. Yanase, F. Nabeshima, Y. Imai, A. Maeda, and S. Tajima, Phys. Rev. B **95**, 184502 (2017).
[74] H. P. Wang, Z. R. Ye, Y. Zhang, and N. L. Wang, Sci. Bull. **61**, 1126 (2016).